# Influence of the nanostructuration of PVD hard TiN-based films on the durability of coated steel

Philippe Steyer, Alexandre Mege, David Pech, C. Mendibide, Julien Fontaine, J.-F. Pierson, Claude Esnouf, P. Goudeau

# Influence of the nanostructuration of PVD hard TiN-based films on the durability of coated steel

Ph. Steyer [a,*], A. Mege [a], D. Pech [a], C. Mendibide [a], J. Fontaine [b], J.-F. Pierson [c], C. Esnouf [a], P. Goudeau [d]

[a] *MATEIS, INSA-Lyon, bât. L. de Vinci, 21 av. Jean Capelle, F69621 Villeurbanne cedex, France*
[b] *LTDS, Ecole Centrale de Lyon, 36 av. Guy de Collonge, F69134 Ecully cedex, France*
[c] *LSGS, Ecole des Mines de Nancy, Parc de Saurupt, F54042 Nancy cedex, France*
[d] *LMP, Université de Poitiers, bd. P. et M. Curie, BP 30179, F86962 Futuroscope Chasseneuil cedex, France*

The design of thin hard coatings at a nanometric scale is very promising to improve the surface characteristics of coated parts. Unfortunately, most often only one specific property is really enhanced. Besides, the origin of such a "nanostructure effect" remains still not clearly elucidated, and a wider industrial development requires a better understanding of the relations linking structure and functionality.

This paper results from an invited review presented within the framework of the EMRS 2007 spring meeting. Its objective is to present how it is possible to control the films structure to achieve optimized performance in terms of tribological, mechanical, and physico-chemical behaviours. Two types of films architecture are studied, resulting either from a stratification of nanolayers, or from a nanodistribution of a crystallised phase into an amorphous matrix. To illustrate both structures, arc-evaporated nanomultilayered TiN/CrN and TiSiN nanocomposite coatings are more particularly developed, and compared to TiN, CrN and $SiN_x$ references.

High wear resistance of TiN/CrN is explained by an original propagation mode of the cracks due to a fluctuating residual stress field, evidenced by TEM and synchrotron measurements. Corrosion behaviour depends mainly on the nature of the outer layer. An external CrN layer, presenting a p-type semiconductive character, affords an enhanced protection. A beneficial role of the nanostratification, susceptible to strongly improve the density of films, was also evidenced. The high oxidation resistance of TiSiN is attributable to the network of refractory $SiN_x$, which acts as a diffusion barrier for oxygen and insulates the highly reactive TiN nanograins from the aggressive atmosphere.

*Keywords:* PVD nanostructured coatings; TiN; Durability; Corrosion; Wear; High temperature oxidation

## 1. Introduction

Transition metal nitrides have been widely used for years as protective coatings to improve the surface characteristics of cutting tools. The most commonly studied PVD thin films are TiN and CrN. However, the requirements in many applications are today so high that classical single-layered hard coatings cannot satisfy them anymore.

Mechanical properties, and hardness especially, were long considered as the key parameters to optimise in order to improve the lifetime of a coated part. Nowadays coated tools have not only to fulfil high mechanical properties, but also have to resist to their potentially aggressive operating environments: industrial atmospheres, lubricant and cooling solutions, high temperatures in dry machining… The physico-chemical behaviour of the part cannot be then neglected anymore. The durability today becomes preponderant and substitutes for the traditional monofunctionality. The notion of durability gathers the main different degradation modes of a coated tool in service i.e. corrosion, wear and high temperature oxidation in particular.

Luo et al. distinguish, from an historical point of view, three different steps in the evolution of the improvement of the durability, corresponding to a more and more complex structuration of the coating [1]. The first one concerns a modification of the chemical nature of single-layered films. For instance, aluminium enrichment to TiN can be highlighted as

* Corresponding author.
*E-mail address:* philippe.steyer@insa-lyon.fr (Ph. Steyer).

this ternary TiAlN coating opened, fifteen years ago, new perspective in the field of high temperature machining. Another solution to increase the durability may consist in modifying the coating architecture by adding different layers, with the objective that each layer affords its specific functionality. As an example, steel coated by a duplex electroless Ni/arc-evaporated CrN benefits simultaneously from the high corrosion resistance due to the Ni defect free sublayer, and from the better tribological behaviour provided by the CrN top-layer [2]. Similarly, improvement of the tribocorrosion behaviour of steel can be reached with the use of a duplex $SiC_x$/DLC film for which DLC topcoat significantly limits the wear, while $SiC_x$ sublayer plays the role of a barrier layer against corrosion [3–5]. The last solution to improve the lifetime of coated parts concerns a modification at a nanometric scale of the distribution of the different phases in the coating, with the aim of hugely increasing the number of interfaces. Indeed, according to Veprek and Reiprich [6], outstanding properties can be reached if the coating is built at a nanometric scale. Two configurations lead to such performance: either by a 3-dimensional dispersion of nanocristallized particles into an amorphous matrix (nanocomposite coating) [7–9] or by a 2-dimensional stratified structure of a few nanometers in thickness layers (nanomultilayered coating or superlattice). Increase in hardness when compared to single-layered coatings has been often reported [10–12] and some explanations of this hardening are based on the *Hall–Petch effect*, on the variations of shear modulus or on internal stresses [13–16]. This hardening could be at the origin of the enhancement of wear resistance of superlattices, whereas for other authors, the key parameter would rather be the ratio of hardness ($H$) of the layer over its elastic modulus ($E$) [17–19]. Recently, Luo et al. demonstrated through TEM observations the beneficial effect of the stratified structure on the resistance of the coating against cracking [1].

If the study of mechanical properties associated to a nanostructuration of coatings is well documented, the role of the environment is often neglected. The aim of this paper, corresponding to an invited review presented at the European Materials Research Society spring meeting (2007), is to enlarge the problem of durability by considering also the behaviour of coated parts in terms of their corrosion and oxidation resistances. Both types of coatings were studied: nanolayered TiN/CrN films as well as TiSiN nanocomposite films. In order to emphasize the role of the nanometric scale structure, a methodology based on the comparison of the behaviour of nanostructured films with that of the corresponding individual monophased references (TiN, CrN and $SiN_x$), was adopted.

## 2. Experimental

### 2.1. Coatings deposition

Coatings were deposited for all experiments on flat M2 tool steels, and on Z200C12 steel balls specifically for tribological tests. Other films were also deposited on glass strips for the determination of their intrinsic electrochemical behaviour. The main deposition parameters are gathered in Table 1, and more details can be found in Refs. [20–22]. For TiSiN nanocomposite film, a sintered $Ti_{0.8}Si_{0.2}$ target was used in a reactive nitrogen atmosphere, while for other samples only pure targets (chromium and titanium) were utilized. For nanolayered films, the period thickness was mainly controlled by the substrate holder rotation speed. For TiN/CrN films deposited by the arc evaporation process in an industrial reactor, samples characterized by bilayer periods ranged between 10 and 60 nm were investigated. Nevertheless, only the period of 40 nm, achieving the best characteristics, is mainly considered in this study.

### 2.2. Physical characterization

Crystallographic structure of coatings was investigated by X-ray diffraction in $\theta/2\theta$ mode and in grazing incidence (0.7°). The crystalline size was estimated from the full width at half maximum of X-ray diffraction line using the Scherrer's formula. Microstructural observations were carried out by scanning electrons microscopy (SEM) equipped with EDS analysis, using a JEOL 840ALG apparatus, and by transmission electrons microscopy (TEM) using a JEOL 200CX one. Thin foil specimens devoted to cross sectional observations were prepared by focused ion beam (FIB) method. This technique consists in extracting, inside a SEM, thin foils by using a gallium ion beam as a cutter.

Hardness and elastic modulus were measured by nanoindentation (MTS Nano II) in continuous stiffness mode. This procedure was applied for all the coatings: the load rate varied between 1 and 15 nm/s with a 1 nm amplitude modulation at 45 Hz. The load is 1 nm/s at the beginning of the measurement, and then continuously increases with the increasing investigated depth. With such a procedure, the deformation rate is constant, so that both hardness and Young modulus values determined for low thicknesses are little scattered. Penetration depth was lower than one tenth of the film thickness in order to minimize the substrate influence on the measured properties.

### 2.3. Electrochemical characterization

Electrochemical measurements were carried out in a standard three-electrode cell with a saturated calomel reference electrode (SCE). Measurements were carried out after 1 h stabilisation, with a M273 PARSTAT potentiostat. Tests were performed in an aerated 0.5 M NaCl solution at room temperature. Polarization

Table 1
Range of deposition parameters used for single-layered and nanostructured coatings

| Arc-evaporated films | | | | |
|---|---|---|---|---|
| Substrate bias (V) | Target evaporation intensity (A) | $N_2$ pressure (Pa) | Deposition time (min) | Thickness (μm) |
| −80 to −150 | 80 to 110 | 1 to 4 | 90 to 120 | 3–5 |
| **Magnetron sputtered films** | | | | |
| Substrate bias (V) | Cathodic power (W) | N2 flow (sccm) | Chamber pressure (Pa) | Thickness (μm) |
| −50 to −125 | 560 to 1800 | 5 to 16 | $10^{-3}$ | 3 |

curves were recorded at 10 mV/min from −200 mV/$E_{corr}$ to +200 mV/$E_{corr}$. Mott–Schottky treatment was applied to coatings deposited onto glass, after an anodic polarization at + 250 mV/sce for 1 h. Interfacial capacitance was then measured at the frequency of 1 Hz with a potential modulation of 15 mV. Due to the galvanic coupling involved between the corrodible substrate and the noble coating, steel may corrode through the open defects allowing the penetration of the electrolyte to the steel. The porosity rate is then a key parameter to determine. Emerging porosity rate was evaluated using the polarisation curves cross-checking method [23]. This method is based on the ratio of the corrosion current density $i_g$ of the coated part over the bare substrate one at the mixed potential $i_a(E_m)$. The porosity rate $p$ defined as the exposed surface in contact with the electrolyte is:

$$p(\%) = i_g/i_a(E_m) \times 100 \quad (1)$$

### 2.4. Tribological characterization

Tribological behaviour of the coatings was investigated through two different set-ups: sliding wear resistance was evaluated with a ball-on-disk tribometer, while surface fatigue resistance was determined by a cyclic multi-impact device. Wear tests were carried out using a ball-on-disc tribometer. Some preliminary experiments using $Si_3N_4$ or sapphire ball sliding on coated steel have been carried out showing the difficulty to quantify the wear of such hard coatings, worn volume of the ball being much more important than the one measured on the studied sample counterpart. A specific configuration was thus adopted: a coated ball (10 mm in diameter) was rubbed against an uncoated disc. Another advantage of this modified configuration is to be more representative of cutting applications. To compare the wear resistance (in a mild wear regime) of different coatings, the evolution of the worn volume $V$ of each coating was plotted versus the cumulative dissipated energy $E_d$. Each point on such plot corresponds then to one experiment performed at a given load (7.5 and 17.5 N) and for a given duration (5 to 60 min) at a sliding speed of 13 cm/s. The dissipated energy first proposed by Mohrbacher et al. [24] has been calculated for each test with the following formula:

$$E_d = \sum \vec{F} \cdot \vec{d} = v \cdot t \cdot \sum F_t \quad (2)$$

where $F_t$ is the tangential force (N), $d$ the sliding distance (m), $v$ the linear speed (m/s) and $t$ the experiment duration (s).

Besides, surface fatigue resistance was estimated by a cyclic impact test [25]. This test consists in repetitively stressing the surface of samples with impacts delivered by a cemented carbide tip having a 300 μm radius of curvature. Energy delivered at each impact (0.8 mJ) was controlled by an electromagnetic propulsion system. Each sample was subjected to 10 to 10,000 successive impacts in air. To enhance the severity of these tests, M2 steel substrate was not thermally hardened on purpose, in order to obtain a higher substrate deformation, hence exposing the films to larger strains.

In order to correlate the tribological properties with the stresses developed in the films, further stresses measurements were carried out at the LURE synchrotron radiation (Orsay, France) at the beam line H10 in asymmetric mode for recording the (200) and/or (220) diffraction peaks, selectively in TiN and CrN layers. A 4-circles goniometer was used for applying the $\sin^2\psi$ method in the $\psi$ configuration. A wavelength of 0.253 nm has been chosen in order to shift the fcc $2\Theta$ diffraction peaks position towards large angles for improving the accuracy of the measurements. $\sin^2\psi$ method, more developed in references [26], consists in using interreticular distance as a strain gauge. Varying the $\psi$ angle of measurement between the normal to the surface and the normal to the (hkl) diffracting planes enables to measure the strain in different grain orientation for the same <hkl> direction and thus to follow the shift of the diffraction peak position due to in plane macro stresses.

### 2.5. High temperature oxidation characterization

Oxidation qualitative tests were performed in air using a conventional furnace at 700 °C during 2 h. After oxidation, the films were analysed by X-ray diffraction in $\theta/2\theta$ mode to study the structural evolution of the remaining Ti–Si–N film and in grazing incidence to study the nature of the oxide layer. The oxide layer thickness was determined using the Calotest® method. Further more discriminating quantitative tests were also performed in a Setaram 92 thermobalance, using dry air as oxidative atmosphere: an isothermal test at 800 °C during 2 h to assess oxidation kinetics, and a dynamic heating from the room temperature up to 1100 °C with the purpose of determining the temperature at which oxidation begins. To extract from each thermogram the value corresponding to the oxidation temperature, a mathematical approximation based on the non-linear least square was applied. In this iterative method the calculated values resulted from an exponential model using two parameters [27].

## 3. Results and discussion

### 3.1. Electrochemical behaviour

#### 3.1.1. Enhancement due to nanostratification

The role of the electrochemical behaviour of coated steel was first evaluated by potentiodynamic curves (Fig. 1). It appears

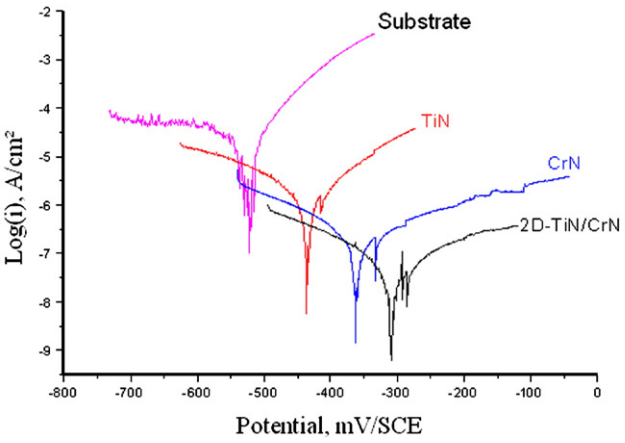


Fig. 1. Potentiodynamic curves of the different samples.

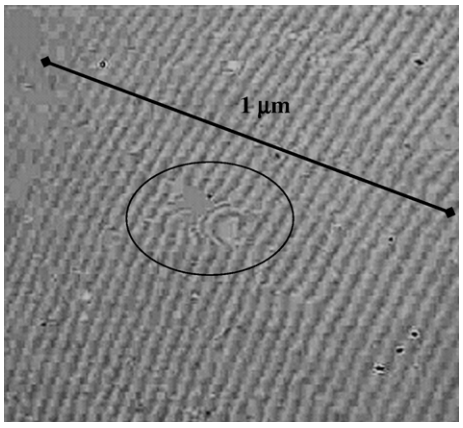


Fig. 2. Metallographic observation of the nanostratified TiN/CrN coated steel in a zone submitted to Calotest characterization. Circled area evidences the effect of a droplet on the growth of coating.

that whatever the sample, a beneficial effect of the coatings is evidenced with corrosion rates slightly lowered for TiN and significantly reduced of about 2 decades for both CrN and nanostratified TiN/CrN films. Besides, coated parts denote from an electrochemical ennoblement which suggests that, as expected, ceramic coatings behave as cathodic materials. Open porosities and pinholes in coatings can form direct paths between the corrosive environment and the substrate, which can lead to a rapid localised galvanic attack of the steel.

The consequences of the galvanic coupling depend on two parameters: the area of substrate in contact with the solution on the one hand, and the electric character of the coating itself on the other hand. This two characteristics have been more deeply investigated.

Emerging porosity rate was evaluated by electrochemistry. We measured porosity rates of 0.2, 0.03 and 0.006% for respectively the TiN, CrN and TiN/CrN coated substrates. Such tiny porosity rates, for the nanostratified coating especially, could be at the origin of its high protection character. We explain such high covering rates by the progresses made last decade in the control of the processes. In particular, the weak amount and the little size of droplets emitted during the deposition would be responsible for the high quality of the layer. Fig. 2 shows for example the surface of the TiN/CrN films after a Calotest measurement. In the circled zone, a little droplet is evidenced. Unlike big traditional droplets for which the growth is dramatically affected, it is shown for the nanolayered film that after about 5 periods the penalising effect of the droplet is cancelled, and the growth unmodified.

### *3.1.2. Prominent role of top-layer*

Another important result can be inferred from Fig. 1, which could account for the supremacy of the nanostratified films regarding corrosion protection. The anodic part of the potentiodynamic curves relative to CrN and TiN/CrN are similar, suggesting similar electrochemical behaviours. This result has to be correlated with the 2-dimensional structure of the film, composed of an alternation of CrN (24 nm) and TiN (16 nm) layers, and for which an outer thick layer (350 nm) of CrN is deposited for an esthetical purpose. The electrochemical behaviour of the coated steel seems thus to be controlled by the nature of the outer layer. In order to determine how this top-layer may influence the electrochemical behaviour of the coated steel, further measurements were performed on films deposited by magnetron sputtering on glass substrates, i.e. without any galvanic effect. When immersed in electrolyte, the intrinsic electrochemical potential of these materials sharply decreases then increases, to finally reach a plateau at very high potential values (Fig. 3a). According to Baroux [28], this evolution in three steps would be characteristic of the presence of a passive film onto the surface. Indeed, such surface layers often present semiconductive properties. To verify this assumption, capacitance of anodised TiN and CrN coated glass was measured by electrochemical impedance spectroscopy. Fig. 3b presents the results according to Mott–Schottky's formalism. Variation of $1/C^2$ versus applied potential shows, in both cases, a linear evolution in a wide potential range. This indicates semiconductive properties of the layer in contact with electrolyte [29]. The positive slope of the straight line relative to passivated TiN corresponds to n-type semiconductor, whereas for the oxide formed onto CrN, the negative slope indicates opposite p-type semiconductive characteristics. According to Sato [30], the

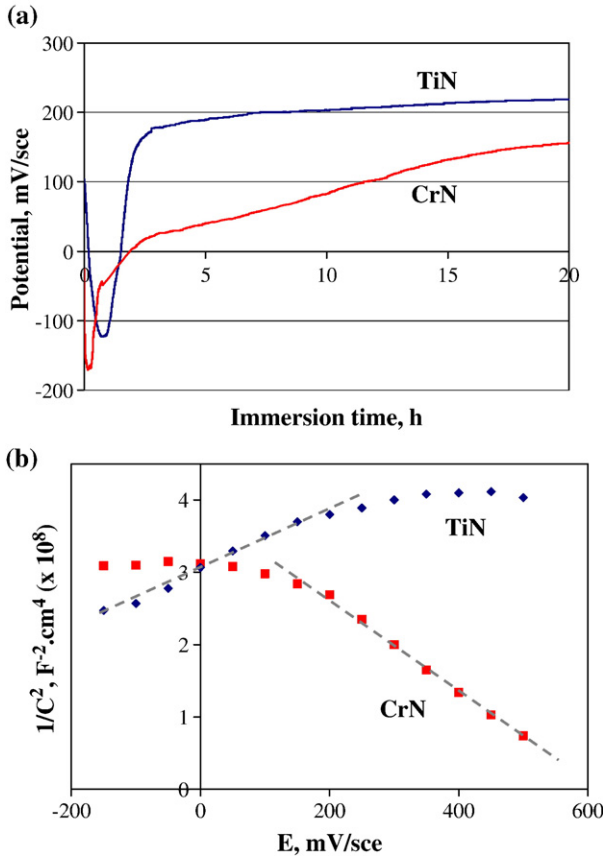


Fig. 3. Electrochemical measurements carried out on both TiN and CrN monolayers deposited onto glass: free corrosion potential versus immersion time (a), Mott–Schottky plots for the pre-oxidized samples (b).

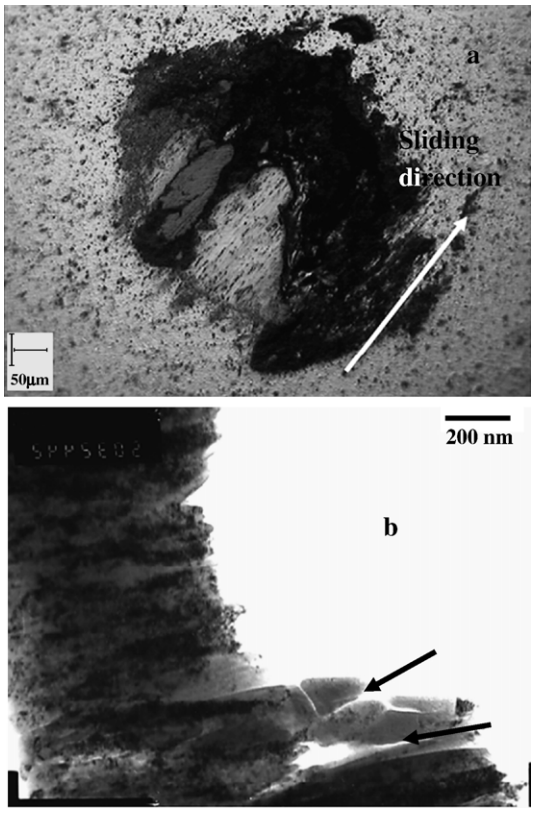


Fig. 4. Observation of the TiN coated steel after the ball-on-disc test in surface (a) and in cross-section (b): TEM bright field image in the wear track (cracks are marked by arrows).

current of a semiconductor resulting from an overvoltage $\eta$ corresponds to:

$$i_n = i_n^0 \cdot (1 - \exp(-K\eta)) \quad \text{and} \quad i_p = i_p^0 \cdot (\exp(K\eta) - 1) \quad (2)$$

respectively for n and p-type semiconductors ($i^0$ being the exchange current of semiconductor and $K$ a constant depending only on the temperature).

Considering the coated part, due to galvanic coupling, coating undergoes an important cathodic overpotential ($\sim -600$ mV). Therefore, in case of n-type semiconductor (passivated TiN) the cathodic current is very high (exponentially increased with overvoltage), while the one of passivated CrN is extremely low and constant ($\sim 10^{-8}$ A/cm$^2$). Owing to the difference of potentials between coatings and substrate, the dissolved oxygen is reduced on the cathodic coating, while emerging substrate corrodes. Since kinetic of cathodic reaction onto passivated TiN is high, concomitant iron dissolution will be important. On the contrary, thanks to its p-type semiconductive properties, passivated CrN results in a very low cathodic current leading to a low corrosion rate.

To sum up, the nanostratified structure plays a double role on the corrosion protection of steel: on the one hand, the nanometer scale structure improves the quality of the film reducing hugely the open-porosity rate; on the other hand it has been established that the electrochemical behaviour of the nanomultilayered coating is governed by the outer layer in contact with the electrolyte. For a better corrosion resistance a topcoat of CrN characterized by favorable semiconductive properties is thus recommended.

### *3.2. Tribological behaviour*

#### *3.2.1. Enhancement of sliding wear resistance*

The same TiN/CrN multilayered coating was compared to TiN and CrN single-layered with the purpose of determining how the nanostratification may modify the tribological behaviour. Taking into account preliminary results evidencing the very high wear resistance of nanostructured coatings, an original configuration of ball-on-disk tests was adopted, for which the coated ball rubbed against the uncoated M2 disc. With such a configuration the wear conditions are more severe for the coating, which is submitted to continuous sliding throughout the test. Different behaviours between single- and multilayered coatings can be distinguished. Concerning single-layered ones and after variable test durations, the peeling of the deposit occurs (Fig. 4a). Spallation initiates in front of the contact, where the tensile stresses are the highest for the ball. TEM observations of the wear scar of TiN coated ball (Fig. 4b) show some cracks along the columnar grain boundaries (highlighted by arrows). The deep degradation results from a crack propagation perpendicular to the substrate plane, leading to the formation of large debris. On the contrary, no coating spallation is observed for the nanomultilayered films. Moreover, a TEM cross-section of the worn 40 nm TiN/CrN coating (Fig. 5) shows longitudinal cracks localised along the interface between the layers. The wear of the multilayer seems thus to be governed by a different cracking mechanism compared to single-layered ones as already demonstrated in the case of TiAlN/CrN superlattice [1]. Wear can also be quantified by the specific wear energy (SWE), which corresponds to the inverse of the slope of the worn volume versus dissipated energy line [31]. Indeed, this parameter presents the advantage of allowing the comparison of tests performed under different loads, and indicates the energy required to wear a given volume of material: at a high SWE corresponds a high wear resistance (Table 2). In accordance with the literature, it is confirmed that

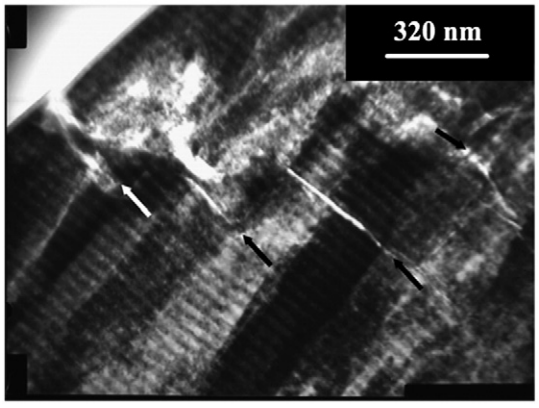


Fig. 5. Bright field TEM cross-section of the worn TiN/CrN coated steel in the wear track (cracks are marked by arrows).

Table 2
Characteristics of the films: mechanical properties, stress state and tribological measurements

| | Hardness (GPa) | Reduced elastic modulus (GPa) | Ratio $H/E$ | Stress (GPa) | Specific wear energy ($mJ/\mu m^3$) | Nb of impacts before delamination |
|---|---|---|---|---|---|---|
| Single-layered TiN | 25 | 305 | 0.082 | −1.8 | 15 | 500 |
| Single-layered CrN | 19 | 250 | 0.076 | −3.0 | 4.5 | 100 |
| Multilayered TiN/CrN | 23 | 290 | 0.079 | TiN layers: −4.7<br>CrN layers: −2.7 | 29 | 4000 |

the wear resistance of TiN, which is harder, is higher than that of CrN, which is softer. More interesting is the value of specific wear energy measured for the nanostratified coating, which is six times higher than the CrN reference coating and two times higher than the TiN reference coating.

*3.2.2. Enhancement of surface fatigue resistance*

Degradation assessed in contact fatigue tests is the consequence of repeated impacts delivered at the coated surface by a hard tip. Considering the small thickness of all the studied coatings (5 μm) compared to the important radius of the tip (300 μm), it can be considered that the maximal shear stress is concentrated within the substrate. This shear stress submits the steel substrate to a plastic deformation, which induces a local bending of the coating, and finally leads to the delamination of the layer. A simple way to evaluate spalling resistance of the coatings is to determine and compare the critical number of impacts required to evidence such delamination (Table 2). Impact experiments show that a significant enhancement of the spalling resistance of nitride coatings can be reached by using a nanomultilayered thin films. Indeed, while single-layered nitrides suffer from delamination after only some hundreds of impacts, the stratified coating resists to 4000 impacts.

*3.2.3. Absence of hardness improvement*

The overall wear behaviour of the nanostructured coatings is thus far better than that of its individual constitutive single-layered coatings. According to the literature, many authors attribute the tribological properties enhancement of nanostructured coatings to a modification of their mechanical properties. In order to verify this assumption for these nanometer scale multilayered coatings, both hardness and elastic modulus were measured by nanoindentation and reported in Table 2. The $H/E$ ratio is approximately the same for all coatings. Therefore, no direct relations between hardness or $H/E$ ratio and the wear resistance can be evidenced. Another explanation to account for such differences in the tribological behaviour of the different coating, could be the formation on surface of a transfer film showing some lubricant properties. The parameter susceptible to prove the occurrence of such a sliding layer is the friction coefficient, measured during the test, and which is ranged between 0.6 and 0.7 whatever the nature of the coating. Anyway, the interest of the specific wear energy to quantify wear resistance is precisely to include differences in sliding coefficient of friction, which may indeed decrease severity of the tests in case of build-up of lubricant layers. So, neither the mechanical properties, nor the sliding nature of the surface can be responsible for the supremacy of nanostructured film regarding their tribological behaviour.

*3.2.4. Prominent role of crack propagation and stress field*

Our interpretation favours the role of the cracking mechanism, which seems to be drastically changed between single- and nanolayered films. The dynamic of cracks depending mainly on the stress field in the films, further stress information are required [15,32–34]. In the case of nanolayered films, the stresses profile is complex to determine, owing to the coherency of the layers, their texture and grains size. Stresses measurements were then carried out with synchrotron radiation by applying the $\sin^2\psi$ method. Results are given in Table 2. All the determined in plane residual stresses are compressive, with a residual stress state higher for

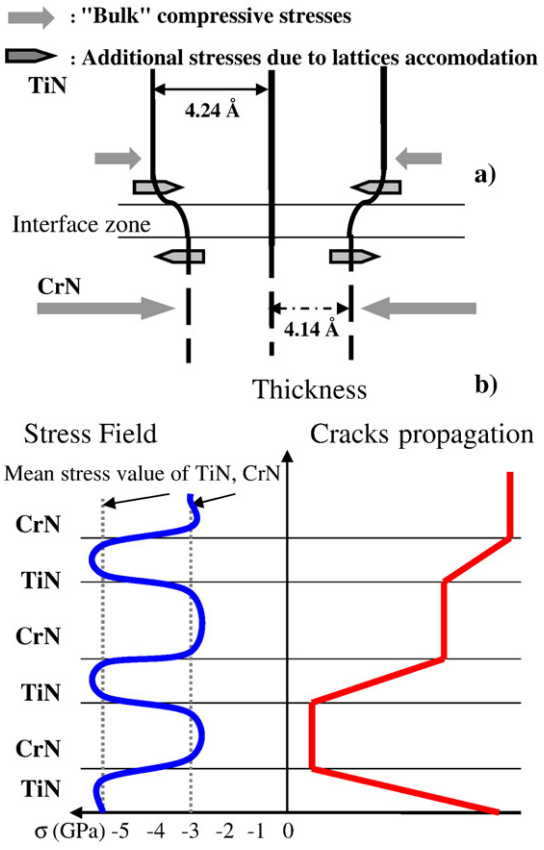


Fig. 6. Role of the lattice parameters accommodation on the fluctuating stress field developed along the coating thickness of nanolayered TiN/CrN films (a), and its consequences regarding the cracking mechanism (b).

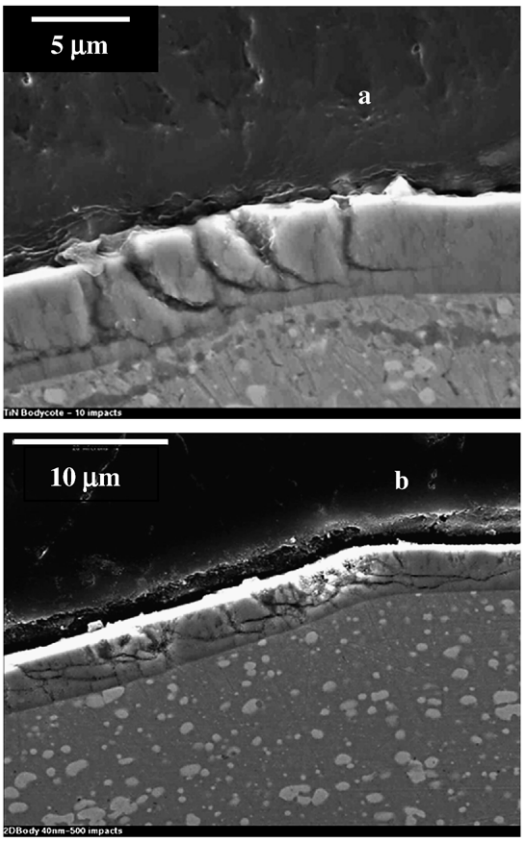


Fig. 7. SEM cross-section micrographs of single-layered TiN (a) and multilayered TiN/CrN (b) after 10 and 500 impacts respectively.

single-layered CrN coating that for TiN one. Surprisingly, results obtained for the same layers involved in the nanostratified structure are really different. The compressive stresses are huge for TiN layers, while they are significantly decreased for CrN ones. In our interpretation, such difference in stress states of TiN and CrN involved either in single- or in multilayered structure could be explained on the basis of a lattice parameters accommodation. Indeed, it has been demonstrated that, on the one hand, both fcc nitrides form by epitaxy [20], and on the other hand their parameters are very close. Therefore, if we focus on the TiN/CrN interface zone (Fig. 6a), TiN layer ($a$=4.24 Å) generates a tension of the CrN lattice ($a$=4.14 Å), while CrN layer provokes a compression of the TiN one. Then, for TiN, CrN layers induce a further compressive component, which has to be added to its initial "bulk" stresses, explaining its outstanding compressive state. In the same way, CrN is submitted to a tensile component by TiN, which reduces its value of compressive stresses, as confirmed by $\sin^2\psi$ measurements. These successive changes of compressive stresses generate a fluctuating stress field all along the film thickness (Fig. 6b) [35]. In the case of single-layered films, cracks can then propagate through the film perpendicularly to the substrate/coating interface until reaching the depth at which stresses are maximal, where they are deviated. This model is consistent with the deviation of cracks for impacted TiN at the approach of substrate, leading to the formation of large adhesive debris (Fig. 7a). In opposite, due to the fluctuating stress field inherent to nanolayered TiN/CrN, the mobility of cracks is strictly modified across each interface. Two different modes of propagation have then to be considered depending on the importance of compressive stresses. Indeed, in CrN layers, which are little stressed, cracks propagate perpendicularly to layers. When this crack reaches the following subjacent TiN layer, which is submitted to a much higher compressive stress state, it is deviated, losing furthermore a part of its original energy. Again, the perturbed trajectories of cracks observed after the fatigue test (Fig. 7b) confirms this particular cracking mechanism. According to this model, each interface may play the role of obstacle, leading to cohesive cracks with emission of only small debris.

The nanostratification of TiN/CrN films greatly improves the tribological properties of coated steel from a wear resistance as well as a surface fatigue resistance points of view. Such enhancement is explained on the basis of an original distribution of stresses all along the film thickness, which favours a less destructive cracking mechanism.

### *3.3. High temperature oxidation behaviour*

#### *3.3.1. Structure of TiSiN films*

Today, with the current development of severe machining, characteristics such as thermal stability and oxidation resistance also become preponderant. Significant progresses in terms of oxidation resistance have then been achieved by addition of elements to TiN [36–38]. In this part, we evaluate the interest on the oxidation resistance of designing films with a nanocomposite structure. TiSiN films deposited by arc evaporation process from a sintered Ti–Si target were considered in this study. Others results concerning a silicon addition by CVD using the silane as Si precursor can be found in ref. [39]. In this study, two Ti–Si–N coatings have been deposited on M2 steel substrates. The Si/Ti atomic ratios determined by EDS are: 0.10 and 0.15. X-ray diffractograms of as-deposited Ti–Si–N coating (Si/Ti=0.1) are presented in Fig. 8a. Whatever the silicon content, only TiN and

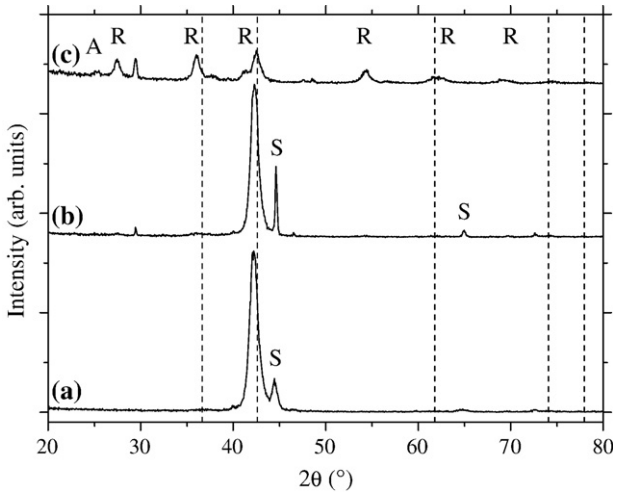


Fig. 8. X-ray diffractograms of the 0.1 Si/Ti ratio Ti–Si–N films (a) as-deposited film, (b) annealed in air at 700 °C and (c) annealed in air at 700 °C and analysed in grazing incidence. Vertical dot lines are related to the theoretical position of TiN diffraction peaks. A, R and S labels are related to diffraction peaks of anatase $TiO_2$, rutile $TiO_2$ and steel substrate respectively.

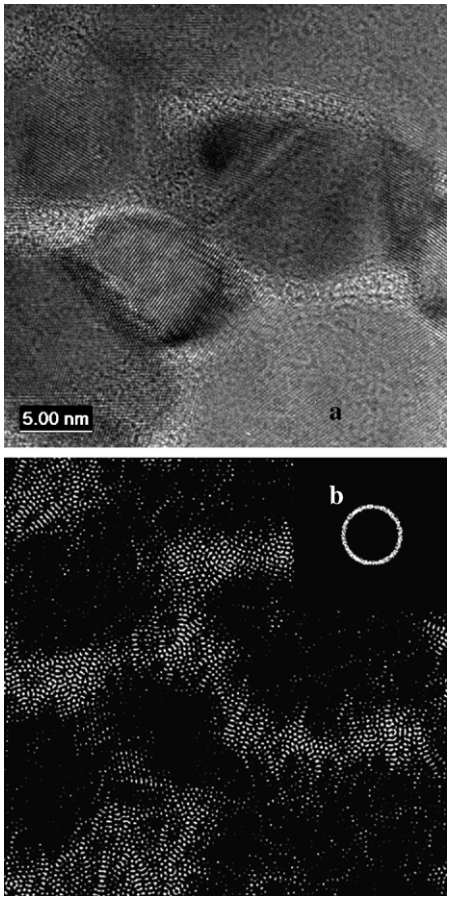


Fig. 9. HRTEM observation of Ti–Si–N film: bright field image (a) and dark field image (b) evidencing the amorphous encapsulating network.

steel substrate diffraction peaks are detected, suggesting that silicon nitride is probably present under an amorphous form. Their mean grains size is ranging between 6 and 8 nm, indicating a nanocrystalline character. The nanocomposite structure is confirmed by TEM observation, which furthermore allows underlining the encapsulation of TiN nanograins by the amorphous matrix (Fig. 9). As a consequence of such a structure, the hardness of both ternary films is higher than 40 GPa. These values are consistent with those published in the literature [40–42] and are very high with respect to TiN (about 29 GPa).

### 3.3.2. Thermal stability of TiSiN nanocomposites

Fig. 8b allows determining the thermal stability of the nanocomposite structure after a high temperature treatment of 2h at 700 °C. When the Si/Ti ratio is 0.10, the diffractogram of the annealed film is very similar to that of the as-deposited film (Fig. 8a). In the same way, the mean grains size remains close to 8 nm. The preserving of the grains size after annealing at 700 °C has to be correlated to the occurrence of the amorphous silicon nitride phase located between TiN grains and which inhibits the growth of grains. For both silicon contents, thickness of the oxide layer is close to 0.3 μm (for comparison, TiN layer is wholly oxidized into rutile). In order to consider more specifically the surface, the films have been analysed in grazing mode (Fig. 8c). Whatever the silicon concentration, X-ray diffractograms are similar: broad peaks of rutile $TiO_2$ are evidenced, indicating that TiN and rutile $TiO_2$ grains exhibits nearly the same grains size. This point, again, confirms the nanocomposite character of the as-deposited Ti–Si–N films.

Table 3
Oxidation parameters of coated and uncoated steel

| | $T_c$ (°C) | $K_p$ (mg cm$^{-2}$ h$^{-1/2}$) |
|---|---|---|
| M2 bare substrate | 510 | 1.11 |
| TiN | 544 | 0.64 |
| Ti–Si–N (Si/Ti=0.10) | 741 | 0.13 |
| Ti–Si–N (Si/Ti=0.15) | 660 | 0.39 |
| $SiN_x$ | 740 | 0.12 |

### 3.3.3. Oxidation resistance of TiSiN nanocomposite

In order to get quantitative information under severe conditions, further experiments have been conducted in thermobalance. Two parameters were measured: the temperature of oxidation beginning, and the kinetic parameter $K_p$, representative of the oxidation rate. The critical temperature, $T_c$, at which oxidation begins has been estimated by measuring the mass variation of the sample as a function of increasing temperatures. All investigated samples show the same evolution, with a wide temperature range without mass variation, followed by an important and rapid mass gain fulfilling an exponential increase. Two series of samples can be distinguished: the bare and TiN coated steels on the one hand, and the other coated parts on the other hand. A direct quantitative interpretation of such curves is difficult owing to the small temperature range within which the two groups of samples oxidize. A mathematical simulation based on the non-linear least square has thus been applied, with the purpose of obtaining objective and accurate values. Results for all samples are gathered on Table 3. As expected, TiN does not really delay the oxidation of M2 steel. Moreover, the critical temperature of TiN (544 °C) is consistent with classical values published in the literature, which validates our mathematical model [38,43]. The low-Si ternary film starts to oxidise at 740 °C, corresponding to the same temperature as $SiN_x$ standard. This might indicate that for such a Si enrichment, the percolation threshold would be reached, as already reported by others authors [44,45].

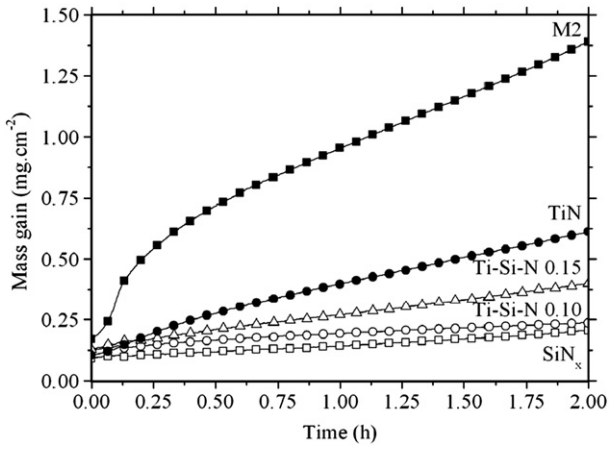


Fig. 10. Thermograms of the different samples obtained at 800 °C for 2 h.

Isothermal thermogravimetric experiments were carried out at 800 °C. Whatever the sample, mass gain evolution versus time shows a parabolic evolution, indicating an oxidation kinetic limited by the diffusion of oxygen (Fig. 10). As in the case of $T_c$ measurements, the same two groups of samples can be again considered regarding their oxidation rate (Table 3). As expected, TiN is characterized by a poor protection against high temperature oxidation (slightly better than the bare steel). On the contrary, for a Si/Ti=0.1 ratio, the Ti–Si–N coated part oxidises five times slower than TiN, which is in agreement with the protective effect reported by other authors [46]. Again the similarity between the values of kinetic constants of both $SiN_x$ and Ti–Si–N (0.13 and 0.12 mg $cm^{-2}$ $h^{-1/2}$ respectively) has to be underlined. The high temperature resistance of Ti–Si–N is then attributable to the intrinsic refractory properties of $SiN_x$, and to its ability to slow down the diffusion of oxygen in particular. Moreover, thanks to the nanocomposite structure, $SiN_x$ network affords a supplementary shield effect, able to prevent penetration of oxidative species to the surface of TiN nanograins.

The poorer refractory characteristics of the richest Si containing film can be explained by the fact that this film presents a thicker $SiN_x$ network. The amount of $SiN_x$ becomes then too high for accommodating the volume variations induced by the temperature changes, which leads to the formation of cracks favouring a deeper oxidation. Such a susceptibility to cracking was already observed in another study focused on the thermal cycling resistance.

To conclude, it has been shown that for a silicon enrichment corresponding to a Si/Ti ratio of 0.1, the promising nanocomposite structure is achieved resulting in high mechanical properties. Furthermore, this structure is preserved at high temperature. Such nanocomposite TiSiN film delays significantly the occurrence of oxidation, which furthermore is greatly slowed down. Such a high temperature protection behaviour is due to the intrinsic refractory character of $SiN_x$ segregated at grains boundaries.

## 4. Conclusion

The objective of this study was to determine the interest, on the durability point of view, to deposit ceramic nitride films at a nanometric scale. Complete durability evaluation must take environmental effects into account. Our analysis was therefore based on the determination of the tribological behaviour of coated steel, together with their physico-chemical characterisation in different aggressive media: corrosion in saline solution, and oxidation in air at high temperatures. Both types of films, nanostratified (TiN/CrN, 40 nm in period) and nanocomposite (TiSiN), were considered.

Concerning corrosion resistance, it has been established that the nanostratified structure affords a beneficial effect by drastically reducing the open-porosity rate, harmful from a galvanic coupling viewpoint. On the other hand, the electrochemical behaviour of the coated part is governed by the outer layer in contact with the electrolyte.

Discriminating pin-on-disk tests as well as oligo-cyclic surface fatigue tests demonstrated the better tribological behaviour afforded by nanolayered TiN/CrN. Such wear resistance is explained thanks to a particular distribution of stresses along the whole film thickness, which would be prone to hinder the propagation of cracks.

Protection against oxidation is strongly improved with ternary TiSiN films: the oxidation temperature is delayed while the oxidation rate is slowed down. Using adequate conditions, we obtain a nanocomposite structure composed of TiN nanograins surrounded by a $SiN_x$ matrix. This structure, stable at temperatures as high as 800 °C, leads to high mechanical properties. The enhanced protectiveness is attributable to $SiN_x$, which affords a double beneficial effect. On the one hand, $SiN_x$ plays efficiently its intrinsic role of diffusion barrier for oxygen. On the other hand, its segregation on the grain boundaries leads to an additional protective shield effect, preventing any contact of the encapsulated TiN with the aggressive atmosphere.

## Acknowledgements

Authors acknowledge for its financial support the *Région Rhône-Alpes* (France) and also are grateful to M. and Mrs Jacquot, M. Damond and M. Héau for the deposition and observation of the different coatings.

## References

[1] Q. Luo, W.M. Rainforth, W.-D. Münz, Wear 225-229 (1999) 74.
[2] P. Steyer, J-P. Millet, S. Anderbouhr, P. Jacquot, Surf. Eng. 17 (2001) 327.
[3] D. Pech, Etude du comportement anti-corrosion de revêtements amorphes base Si élaborés par PACVD, PhD thesis, INSA de Lyon (2006).
[4] D. Pech, P. Steyer, A.-S. Loir, J.-C. Sanchez-Lopez, J.-P. Millet, Surf. Coat. Technol. 201 (2006) 347.
[5] A.-S. Loir, D. Pech, P. Steyer, Y. Gachon, C. Heau, J.-C. Sanchez-Lopez, Plasma Process. Polym. 4 (2007) 173.
[6] S. Veprek, S. Reiprich, Thin Solid Films 268 (1995) 64.
[7] J. Patscheider, T. Zehnder, M. Diserens, Surf. Coat. Technol. 146-147 (2001) 201.
[8] S. Zhang, D. Sun, Y. Fu, H. Du, Surf. Coat. Technol. 167 (2003) 113.
[9] F. Vaz, L. Rebouta, P. Goudeau, J. Pacaud, H. Garem, J.-P. Rivière, A. Cavaleiro, E. Alves, Surf. Coat. Technol. 133-134 (2000) 307.
[10] M. Nordin, M. Larsson, S. Hogmark, Surf.Coat.Technol. 106 (1998) 234.
[11] P. Yashar, S.A. Barnett, J. Rechner, W.-D. Sproul, J. Vac. Sci. Technol., A, Vac. Surf. Films 16 (1998) 2913.
[12] W.-D. Münz, L.A. Donohue, P.E.h. Hovsepian, Surf. Coat. Technol. 125 (2000) 269.
[13] J.S. Koehler, Phys. Rev., B 2 (1970) 547.
[14] X. Chu, S.A. Barnett, J. Appl. Phys. 77 (1995) 4403.
[15] P.C. Yashar, W.D. Sproul, Vacuum 55 (1999) 179.
[16] J. Musil, Surf. Coat. Technol. 125 (2000) 322.
[17] T.L. Oberle, J. Metals 3 (1951) 438.
[18] A. Leyland, A. Matthews, Wear 246 (2000) 1.
[19] C. Rebholz, A. Leyland, J.M. Schneider, A.A. Voevodin, A. Matthews, Surf. Coat. Technol. 120-121 (1999) 412.
[20] C. Mendibide, J. Fontaine, P. Steyer, C. Esnouf, Tribol. Lett. 17 (2004) 779.
[21] C. Mendibide, P. Steyer, J.-P. Millet, Surf. Coat. Technol. 200 (2005) 109.
[22] P. Steyer, D. Pilloud, J.-F. Pierson, J.-P. Millet, M. Charney, B. Stauder, P. Jacquot, Surf. Coat. Technol. 201 (2006) 4158.
[23] J. Creus, H. Mazille, H. Idrissi, Surf. Coat. Technol. 130 (2000) 224.
[24] H. Mohrbacher, J.-P. Celis, J.-R. Roos, Trib. Int. 28 (1995) 269.
[25] A.C. Sekkal, C. Langlade, A.-B. Vannes, Mater. Sci. Eng., A 393 (2005) 140.
[26] C. Mendibide, P. Steyer, C. Esnouf, P. Goudeau, D. Thiaudère, M. Gailhanou, J. Fontaine, Surf. Coat. Technol. 200 (2005) 165.
[27 C.L. Lawson, R.J. Hanson, Solving Least Squares Problems, Prentice-Hall, 1974, p. 337.

[28] B. Baroux, Surface State Model for the Surface Potential of Passive Metal, Pennington, San Antonio, 1996, p. 322.
[29] N. Sato, Electrochemistry at Metal and Semiconductors Electrodes, Elsevier, New York, 1998, p. 400.
[30] N. Sato, Corrosion 45 (1989) 354.
[31] S. Fouvry, P. Kapsa, Surf. Coat. Technol. 138 (2001) 141.
[32] X. Junhua, L. Geyang, G. Mingyan, Thin Solid Films 370 (2000) 45.
[33] Y. Zhou, R. Asaki, W.H. Soe, R. Yamamoto, Wear 236 (1999) 159.
[34] P.B. Mirkarimi, L. Hultman, S.A. Barnett, Appl. Phys. Lett. 57 (1990) 2654.
[35] C. Mendibide, P. Steyer, J. Fontaine, P. Goudeau, Surf. Coat. Technol. 201 (2006) 4119.
[36] C. Heau, R.Y. Fillit, F. Vaux, F. Pascaretti, Surf. Coat. Technol. 120-121 (1999) 200.
[37] K.-S. Lee, S.-M. Seo, K.-A. Lee, Scr. Mater. 52 (2005) 445.
[38] F. Vaz, L. Rebouta, M. Andritschky, M.-F. da Silva, J.-C. Soares, J. Eur. Ceram. Soc. 17 (1997) 1971.
[39] D. Pilloud, J.-F. Pierson, P. Steyer, A. Mege, B. Stauder, P. Jacquot, Mater. Lett. 61 (2007) 2506.
[40] M. Diserens, J. Patscheider, F. Levy, Surf. Coat. Technol. 108-109 (1998) 241.
[41] S. Veprek, J. Vac. Sci. Technol., A, Vac. Surf. Films 17 (1999) 2401.
[42] P.J. Martin, A. Bendavid, Surf. Coat. Technol. 163-164 (2003) 245.
[43] Y.-H. Chen, M. Guruz, Y.-W. Chung, L.M. Keer, Surf. Coat. Technol. 154 (2002) 162.
[44] L. Rebouta, C.J. Tavares, R. Aimo, Z. Wang, K. Pischow, E. Alves, T.C. Rojas, J.A. Odriozola, Surf. Coat. Technol. 133-134 (2000) 234.
[45] A. Niederhofer, T. Bolom, P. Nesladek, K. Moto, C. Eggs, D.S. Patil, S. Veprek, Surf. Coat. Technol. 146-147 (2001) 183.
[46] M. Diserens, J. Patscheider, F. Levy, Surf. Coat. Technol. 120-121 (1999) 158.